Hindawi
Wireless Communications and Mobile Computing
Volume 2022, Article ID 9663091, 8 pages
https://doi.org/10.1155/2022/9663091

Research Article

Research of Crack Defect Detection in Metal Pipes Based on Microwave Antenna Array

Guohua Qiu, Shanshan Tian, and Qinwen Yuan

Key Laboratory of Electromagnetic Wave Information Technology and Metrology of Zhejiang Province, College of Information Engineering, China Jiliang University, Hangzhou, 310018 Zhejiang, China

Correspondence should be addressed to Guohua Qiu; ghqiu@cjlu.edu.cn

Received 24 June 2022; Revised 26 July 2022; Accepted 28 July 2022; Published 13 August 2022

Academic Editor: Chia-Huei Wu

This study evaluates the feasibility of using antenna array to detect crack defects in metal pipes. Antenna arrays are set at the port of a metal pipe in radial direction, and the microwave signal can be effectively coupled into the metal pipe. It can produce orbital angular momentum (OAM) waves. The cracks in the pipe will change the microwave transmission characteristics, and they can be inspected by time domain reflectometry (TDR) of vector network analyzer (VNA). By studying the transmission characteristics of current on the inner surface of the metal pipe, the feasibility of linearly polarized TE_{11} mode microwaves for crack inspection was preliminarily verified. Three galvanized metal pipes with an inner diameter of 8 cm and a total length of about 270 cm were used in the experiment. Axial slits and circumferential slits were used to simulate the crack, respectively. The slits penetrated the pipe wall with a breach of approximately 10 cm × 0.7 cm. The experimental results demonstrated that the radial direction antenna array can detect both the axial slit and circumferential slit through TDR and standing wave ratio (SWR) at the port, especially effective for the axial slit. It provides a new inspection method for metal pipe defect evaluation.

1. Introduction

Metal pipes are widely used in various production and life, including gas and oil transportation [1–3]. As many metal pipes have been used for many years, some have potential safety hazards. Leakage of metal pipes can cause economic loss [4–8]. The defect inspection methods of metal pipes mainly include infrared thermal imaging inspection, ultrasonic inspection, eddy current inspection, optical fiber sensing inspection, and microwaves, etc [9–15]. The ultrasonic method is used for internal defect inspection and wall thickness measurement of metal pipes. Eddy current testing is suitable for detecting cracks and changes in pipe wall thickness on the outer wall of a metal pipe [16]. These inspection methods belong to the direct contact inspection method, the testing equipment is complex, and the accurate positioning of defects needs to be improved. As a new inspection technology, microwave inspection technology is receiving increasing attention, and it is widely used in the inspection of buildings and structures [17–19].

The metal circular pipe is a kind of circular waveguide that guides electromagnetic waves. According to the microwave transmission theory, the propagation of the electromagnetic wave in the waveguide mainly depends on the cross-section shape of the waveguide, microwave frequency, and transmission mode. When any of the parameters changes, the propagation characteristics of the microwave will change. If there is a defect, crack, or other material deposition somewhere in the metal pipe, the reflection and scattering of waves will occur here. If the microwave transmits in one mode in a pipe, when there is a crack in the pipe, the crack will cut off the induced current on the inner surface wall, and the electromagnetic field distribution will be distorted. In this study, the research on metal pipe defect detection technology based on microwave antenna array is proposed. A certain number of antennas are placed at the port of the detected pipe, and the microwave can be effectively coupled into the pipe. Pipe defects such as cracks will cause changes in microwave transmission. The microwave can be analyzed by measuring its time or frequency domain

characteristics, so the inspection of metal pipe defects can be realized.

2. Theoretical Analysis

Arrays of the antenna are used to direct the radiated power towards a desired angular sector. There are many types of antenna arrays, and some antenna arrays consist of one-dimensional or two-dimension. The study discusses the radial antenna array, and all antennas are placed in a circle. The nth dipole antenna element is located at $\mathbf{r_n} = a(\mathbf{e_x} \cos \varphi + \mathbf{e_y} \sin \varphi)$, where $a = |\mathbf{r_n}|$ denotes the radius of the antenna arrays, its excitation is $\mathbf{I_n} = \mathbf{d_n} e^{j\Phi n}$, where $\mathbf{d_n}$ denotes the direction of the element, the electrically phased of the nth element is $\Phi_n = l\varphi_n$, where $\varphi_n = 2\pi n/N$ is the angle of the nth element position, and l is the orbital angular momentum mode [20]. The vector potential of the nth dipole antenna can be written as equation (1), the vector potential and the E-field of all antennas array can be expressed by equations (2) and (3).

$$\mathbf{A_n} = \int_0^d \mathbf{d_n} \frac{\mu}{4\pi} e^{jl\varphi_n} \frac{e^{-jk|\mathbf{r}-\mathbf{r_n}|}}{|\mathbf{r}-\mathbf{r_n}|} dl, \tag{1}$$

$$\mathbf{A} = \sum_{n=1}^{N} \mathbf{A_n}, \tag{2}$$

$$\mathbf{E} = -j\omega\left(\mathbf{A}_\theta + \mathbf{A}_\varphi\right). \tag{3}$$

2.1. Theory of the Radial Direction Antenna Array. Figure 1 shows the radial direction antenna array in the cross section of the pipe. The dipole antenna elements are placed radially along the circumference with N equidistant elements. The vector potential for the N antenna elements can be shown in equation (4).

$$\begin{aligned}\mathbf{A_1} = \sum_{\mathbf{n}=1}^{N} \mathbf{A_{1n}} = \sum_{\mathbf{n}=1}^{N} \frac{e^{-jk|\mathbf{r}-\mathbf{r_n}|}}{|\mathbf{r}-\mathbf{r_n}|} \int_0^d \\ \cdot [\mathbf{r}(\sin\theta\cos\varphi\cos\varphi_n + \sin\theta\sin\varphi\sin\varphi_n) \\ + \boldsymbol{\theta}(\cos\theta\cos\varphi\cos\varphi_n + \cos\theta\sin\varphi\sin\varphi_n) \\ + \boldsymbol{\varphi}(-\sin\varphi\cos\varphi_n + \cos\varphi\sin\varphi_n)] \frac{\mu}{4\pi} e^{jl\varphi_n} dl.\end{aligned} \tag{4}$$

Then, the three components can be expressed as equation (5) to equation (7), $e^{jl\varphi n}$ is the factor of orbital angular momentum (OAM), and $J_l(ka \sin\theta)$ is the Bessel function.

$$\begin{aligned}A_{1r} = \sum_{n=1}^{N} A_{1nr} = \sum_{n=1}^{N} \frac{e^{-jk|\mathbf{r}-\mathbf{r_n}|}}{|\mathbf{r}-\mathbf{r_n}|} \int_0^d \\ \cdot [r(\sin\theta\cos\varphi\cos\varphi_n + \sin\theta\sin\varphi\sin\varphi_n)] \frac{\mu}{4\pi} e^{jl\varphi_n} dl \\ = \frac{r\mu d \sin\theta}{4\pi r} e^{jl\varphi} e^{-jkr} \sum_{n=1}^{N} \cos(\varphi_n - \varphi) e^{jl(\varphi_n-\varphi)} e^{jka \sin\theta \cos(\varphi_n-\varphi)} \\ = \frac{rj^{(l-1)} N\mu d \sin\theta}{8\pi r} e^{jl\varphi} e^{-jkr} [J_{l-1}(ka\sin\theta) - J_{l+1}(ka\sin\theta)],\end{aligned} \tag{5}$$

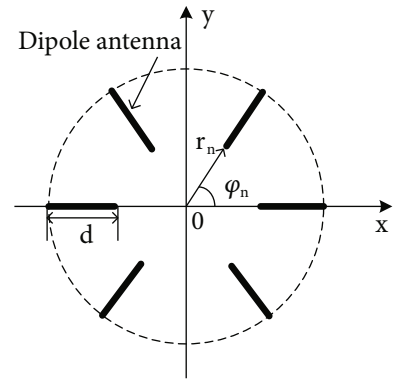

Figure 1: Radial direction antenna array.

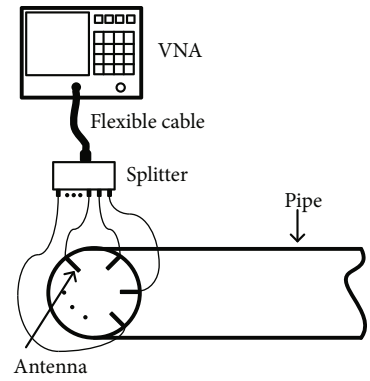

Figure 2: The scheme of experimental system.

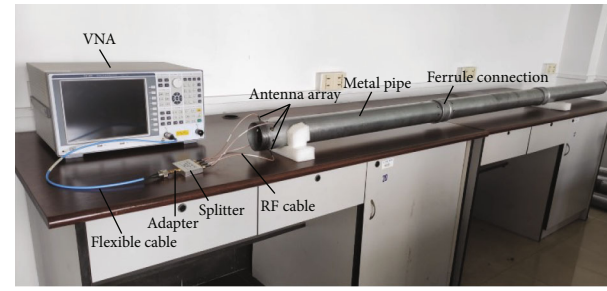

Figure 3: Photo of the experimental scenes.

$$A_{1\theta} = \frac{j^{(l-1)} N\mu d \cos\theta}{8\pi r} e^{jl\varphi} e^{-jkr} [J_{l-1}(ka\sin\theta) - J_{l+1}(ka\sin\theta)], \tag{6}$$

$$A_{1\varphi} = \frac{j^{(l-2)} N\mu d}{8\pi r} e^{jl\varphi} e^{-jkr} [J_{l-1}(ka\sin\theta) + J_{l+1}(ka\sin\theta)]. \tag{7}$$

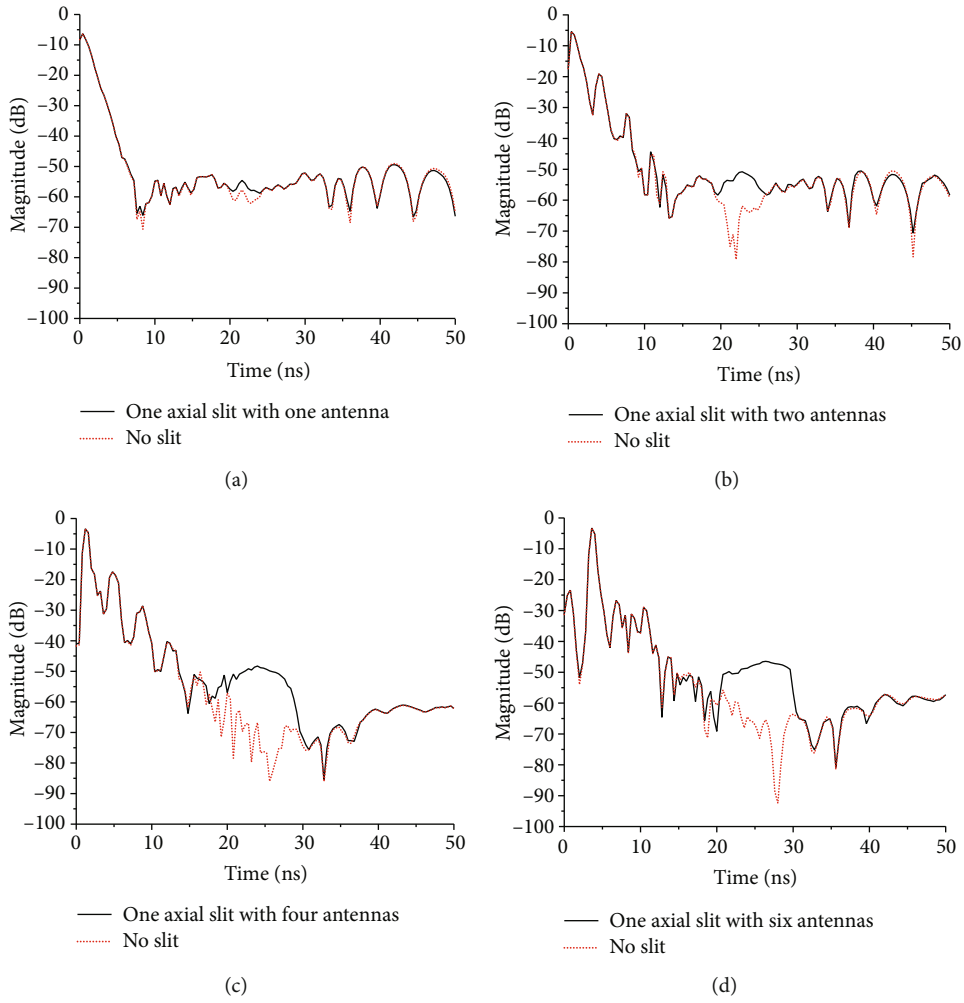

Figure 4: Logarithmic magnitude due to one axial slit with a different number of antennas.

The E-field of the radial direction arrays of antennas is shown in the following equation [21].

$$\begin{aligned}\mathbf{E_1} = &-\frac{j^l N\mu\omega^2 d}{16\pi r}e^{-jkr}\\ &\cdot\left\{\left[(\mathbf{x}-j\mathbf{y})\left(\cos^2\theta-1\right)e^{j(l+1)\varphi}+(\mathbf{x}+j\mathbf{y})\left(\cos^2\theta+1\right)e^{j(l-1)\varphi}-2\mathbf{z}\sin\theta e^{jl\varphi}\right]J_{(l-1)}(ka\sin\theta)\right.\\ &\left.-\left[(\mathbf{x}-j\mathbf{y})\left(\cos^2\theta+1\right)e^{j(l+1)\varphi}+(\mathbf{x}+j\mathbf{y})\left(\cos^2\theta\text{-}1\right)e^{j(l-1)\varphi}-2\mathbf{z}\sin\theta e^{jl\varphi}\right]J_{(l+1)}(ka\sin\theta)\right\}.\end{aligned} \tag{8}$$

2.2. Antenna Arrays Pattern Multiplication. The property of the antenna array is the relative phase shifts in the radiation vector. The array pattern multiplication property can be obtained as shown in the following equation.

$$\mathbf{F}(k) = \mathbf{B}(k)\mathbf{F_n}(k), \tag{9}$$

where $\mathbf{B}(k)$ denotes the array factor, and $\mathbf{F_n}(k)$ denotes the nth radiation vector of the translated current, which are expressed by the following equations.

$$\mathbf{B}(\mathbf{k}) = \sum_{n=1}^{N} b_n e^{j\mathbf{k}\cdot\mathbf{r_n}}, \tag{10}$$

$$\mathbf{F_n}(\mathbf{k}) = \int e^{j\mathbf{k}\cdot(\mathbf{r}-\mathbf{r_n})}\mathbf{J}(\mathbf{r}-\mathbf{r_n})d^3(\mathbf{r}-\mathbf{r_n}). \tag{11}$$

Therefore, the radiation intensity and power gain can be shown as follows:

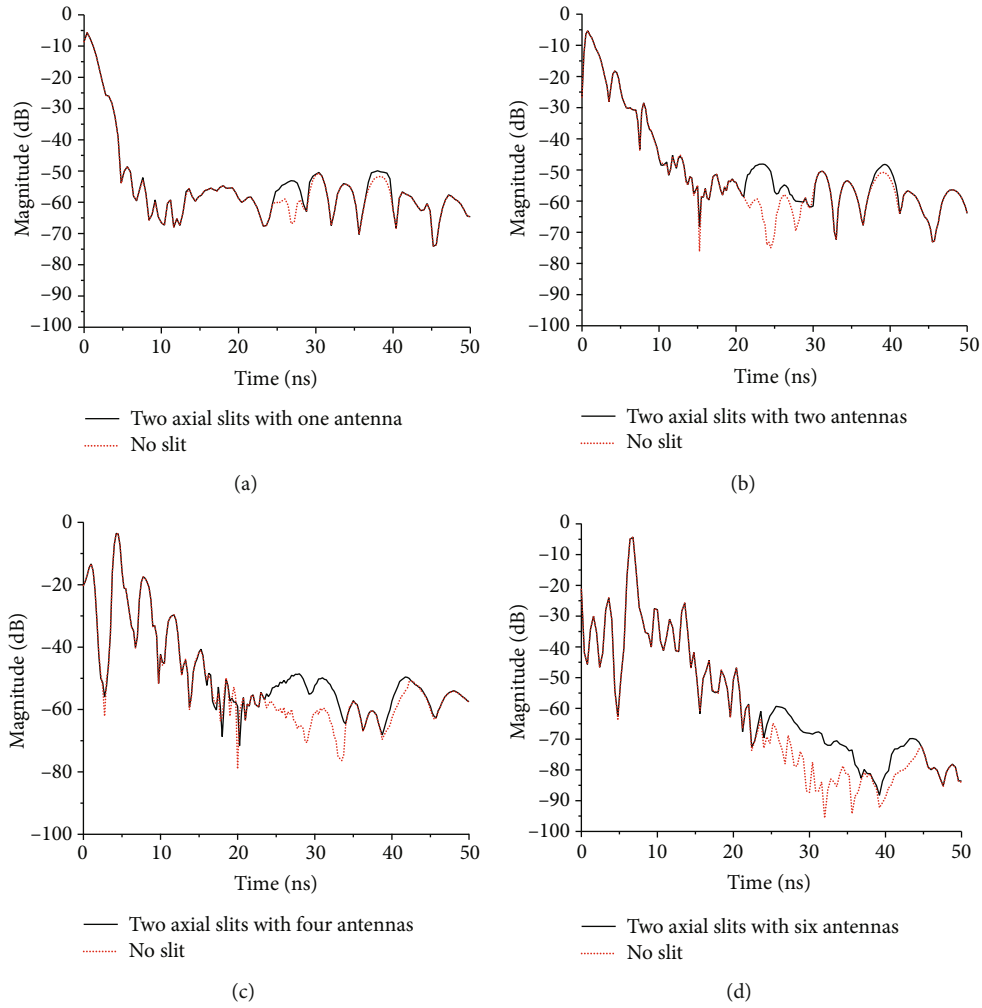

Figure 5: Logarithmic magnitude due to two axial slits with a different number of antennas.

$$\begin{cases} U(\theta,\varphi) = |\mathbf{B}(\theta,\varphi)|^2 U_n(\theta,\varphi), \\ G(\theta,\varphi) = |\mathbf{B}(\theta,\varphi)|^2 G_n(\theta,\varphi), \end{cases} \tag{12}$$

where $U_n(\theta,\varphi)$ and $G_n(\theta,\varphi)$ denote the radiation intensity and power gain of the nth element [22–25].

3. Experimental Approach

3.1. Experimental Setup. The scheme of the pipe defect testing system is shown in Figure 2. The system consisted of a vector network analyzer (VNA), flexible cable, splitter, antenna array, metal pipe, and so on. Figure 3 shows the photo of the experimental scenes. The VNA (Ceyear 3656A) generates microwave whose frequency range to 3GHz. Flexible cable is a stable phase cable which propagates the microwave. Antenna arrays were composed of some rod antennas whose frequency range to 2.7 GHz. The condition for microwave transmission in the pipe is that its frequency was greater than 2.2 GHz. Three kinds of splitter were used in the experiment: one to two, one to four, and one to six. The antenna was connected to the power divider output. The antenna arrays were arranged radially along the metal pipe wall. As shown in Figure 3, the VNA output microwave, the microwave was sent to the flexible cable, then the microwave was input to the splitter, and finally, the array antenna received the microwave and radiated it in the metal pipe. The test adopted a terminal open circuit, which can generate a standing wave in the pipeline for single port detection. As the pipe slits had been processed in advance, each slit was covered with metal sheets to indicate seamlessly. In the experiment, the frequency range was set from 300 MHz to 2.8 GHz to analyze the logarithmic magnitude of port 1 return loss in time domain reflectometry (TDR), and the standing wave ratio (SWR) inspection frequency range was between 2.2 GHz and 2.6 GHz.

3.2. Experimental Materials. Galvanized pipes were used as metal pipes for the test. Because the long metal pipes were difficult to handle, the metal pipes used for the test consisted of three pipes, the length of each pipe was 90 cm, the inner diameter was 8 cm, and the wall thickness was 0.4 mm. The three pipes were connected by ferrule connection. To imitate the cracks in a metal pipe, two types of slits were

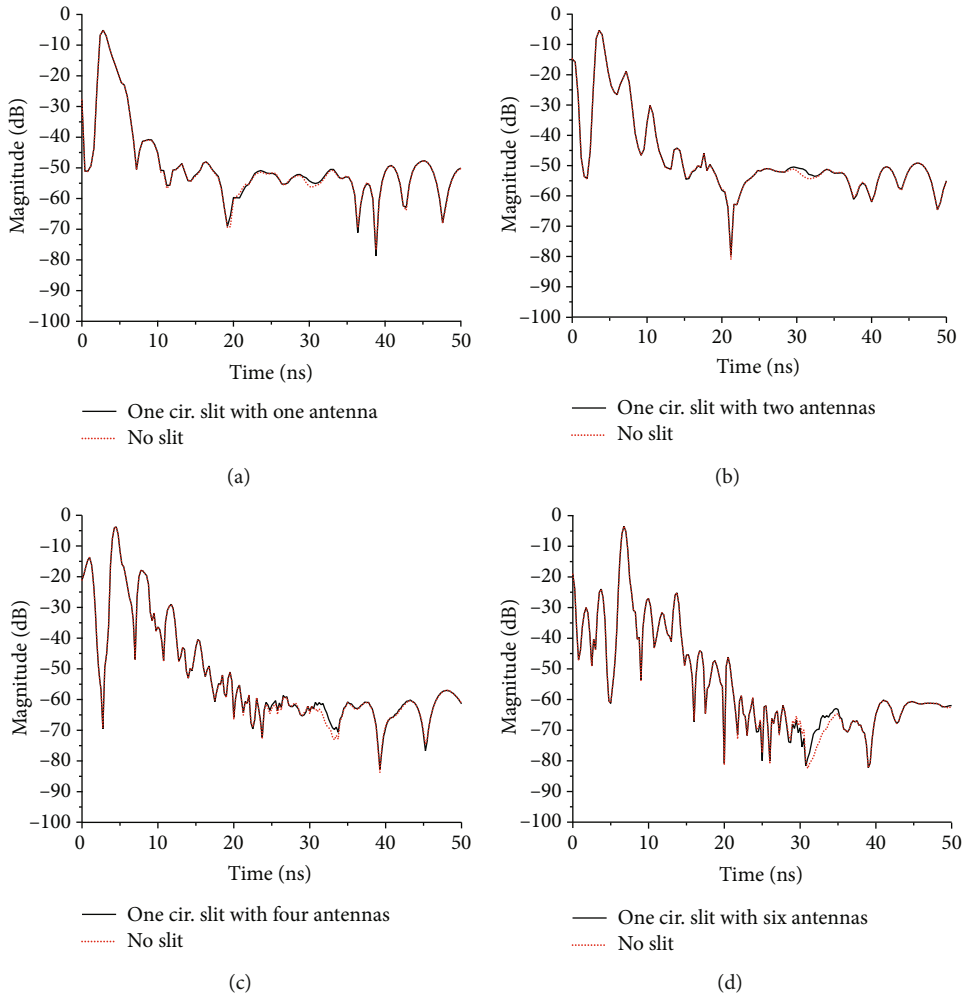

Figure 6: Logarithmic magnitude due to one circumferential slit with a different number of antennas.

manufactured. The slit penetrated the pipe wall with a breach of approximately 10 cm × 0.7 cm, one was an axial slit parallel to the axial direction of the metal pipe, and the other was a circumferential slit which was vertical to the metal pipe. There were four kinds of conditions to detect: the center of an axial slit was arranged along the pipe, about 133 cm away from the pipe input port, the center of one circumferential slit was arranged along the pipe, about 138 cm away from the pipe input port, the centers of two axial slits were arranged along the pipe at 150 cm and 220 cm, and the centers of two circumferential slits were arranged along pipe around at 138 cm and 247 cm. Three types of antenna arrays were used in the experiment: two antennas, four antennas, and six antennas.

4. Results and Discussions

4.1. The Analysis of Logarithmic Magnitude in Time Domain. Figure 4 presents the logarithmic magnitude of an axial slit in the time domain under different antenna arrays. In Figure 4(a), the time domain reflective peak near 0 ns was the port of the pipe where the standing wave was generated. Compared with the two curves in the figure, the logarithmic magnitude of the one axial slit was higher than no slit near 22 ns, this indicated that the return loss occurs here. For other reflection peaks, this was caused by the rough pipe wall and the ferrule connections. In Figure 4(b), the first reflective peak was near 0.5 ns, and there was clearly a logarithmic magnitude change near 23 ns. Because the array was composed of two antennas, each antenna radiated power in a specific direction with a certain magnitude and phase, the relative displacement of the two antennas had a relative phase shift in the radiation vector, and the time domain that caused the change was widened. Thus, there was a different logarithmic magnitude at the open port of the pipe and other places. These phenomena also occurred in Figures 4(c) and 4(d). As shown in Figure 4, the slit is easier to detect with the increase in the number of antennas.

Figure 5 shows the logarithmic magnitude with two axial slits of the antenna array composed of different numbers of antennas. There were similar phenomena in Figure 4. In Figure 5(a), the logarithmic magnitude near 0 ns at the pipe opening was also obvious. At 26 ns and 38 ns, the logarithmic magnitude curve with slits changes compared with no

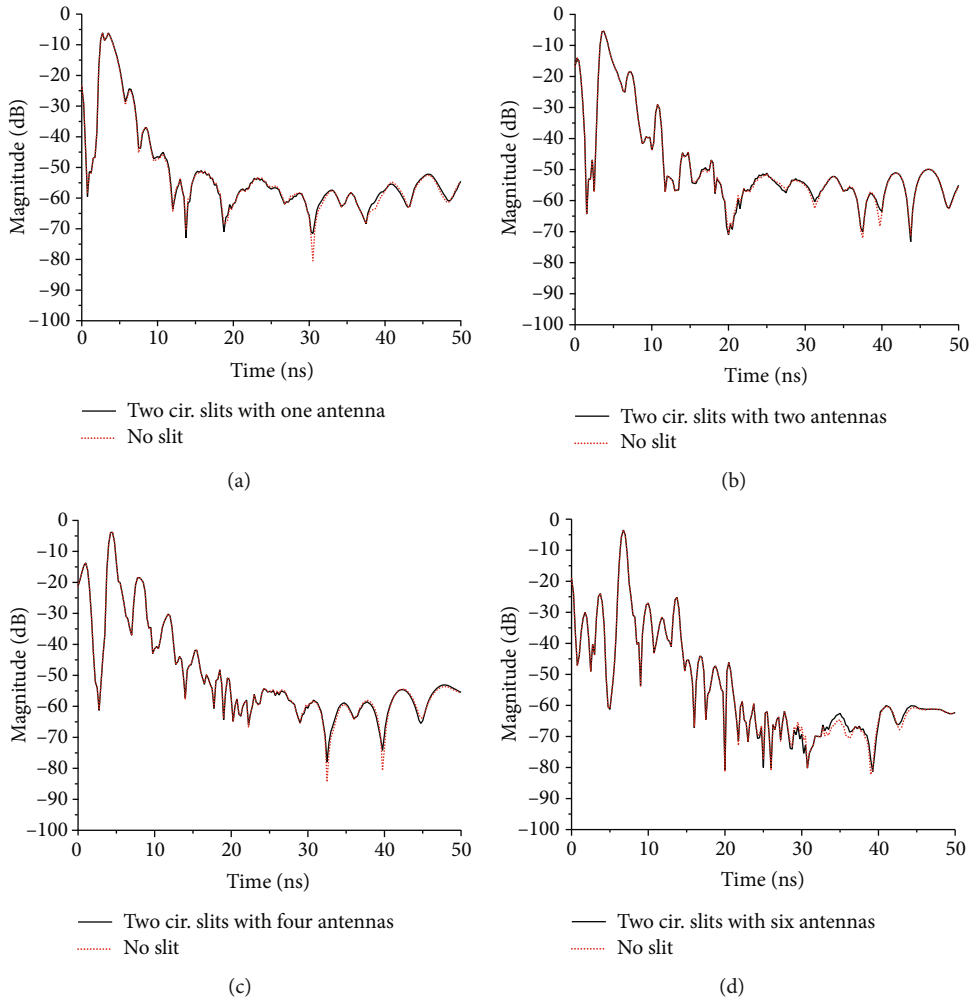

Figure 7: Logarithmic magnitude due to two circumferential slits with a different number of antennas.

slit. The signal leaked more in the first slit than in the second slit, so the logarithmic magnitude of the first changed greater than the second one.

Figure 6 presents the logarithmic magnitude of one circumferential slit in the time domain under different antenna arrays. The reflection of two antennas, four antennas, and six antennas can be observed near 33 ns, but it was not obvious in the case of a single antenna. The time domain logarithmic magnitude is caused by the two circumferential slits as shown in Figure 7. Reflections caused by circumferential slits of four antennas and six antennas were also detected near 30 ns and 40 ns, and it was also not obvious in the case of one antenna. This shows that the antenna array was better than a single antenna.

4.2. The Analysis of SWR. Figure 8 presents the SWR generated by the radiation of metal pipes with an axial slit by different numbers of antennas. The results indicated that the linearly polarized TE_{11} mode can easily test the axial slit centered at 133 cm. The SWR at the axial slit also increased when the number of antennas increased. Figure 9 shows SWR generated by the radiation of metal pipes with two axial slits by a different number of antennas, and a similar

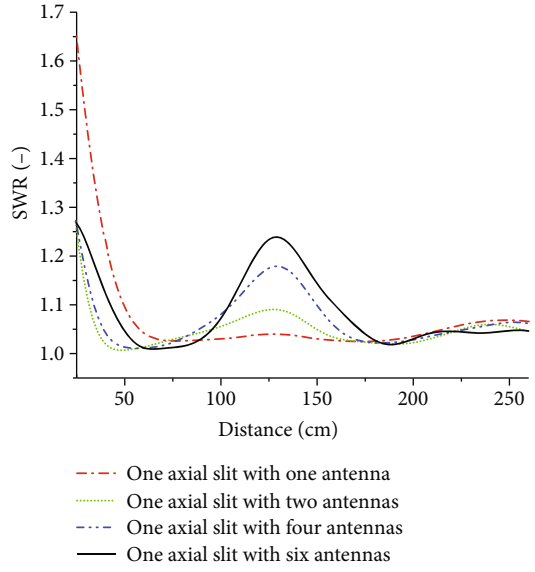

Figure 8: SWR due to one axial slit with a different number of antennas.

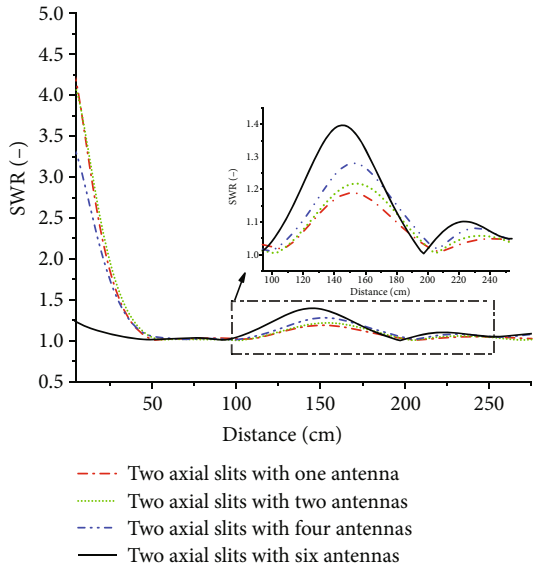

Figure 9: SWR due to two axial slits with a different number of antennas.

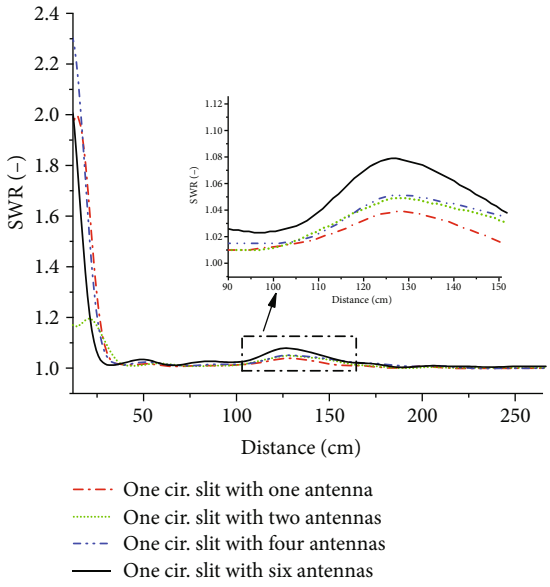

Figure 10: SWR due to one circumferential slit with a different number of antennas.

phenomenon occurred around the two axial slits whosed centers were situated at 150 cm and 220 cm. The SWR of the first axial slit was greater than the second one, which indicated that the TE_{11} mode microwave leaked out the microwave in the first axial slit at 150 cm more than the second one at 220 cm.

Figure 10 shows SWR generated by circumferential slit radiation with a different numbers of antennas. The results show that the antenna array can also test a circumferential slit that employed the linearly polarized TE_{11} mode, while the circumferential slit was located at the center of 138 cm. Figure 11 presents the SWR generated by two circumferential slits for different numbers of antennas. The wave appears

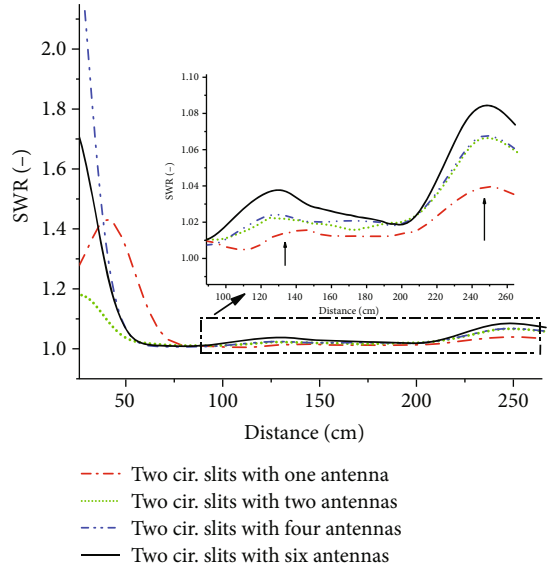

Figure 11: SWR due to two circumferential slits with a different number of antennas.

near two circumferential slits centered at 138 cm and 247 cm.

5. Conclusions

In this research, a certain number of antennas were placed along the radial direction at the port of the tested metal pipe as an antenna array, which can effectively couple the microwave to the metal pipe. The slits in the pipe will change the microwave transmission characteristics. There were three forms of antenna array: two antennas, four antennas, and six antennas. Axial slits and circumferential slits in different locations were designed for four kinds of metal pipes with a length of about 270 cm and an inner diameter of 8 cm. Two methods were used to analyze the defects of metal pipes: one was TDR analysis of microwave logarithmic magnitude at the pipe port, and the other was SWR analysis. According to the experimental results, the information of logarithmic amplitude TDR is relatively rich, SWR is concise, and the performance of the latter is better than the former. Microwave is light-like, and the measurement adopted the single port method, so it can detect long metal pipes. The experimental results demonstrate that the antenna array was helpful for crack detection, and it becomes indeed with the increase in the number of antennas. The radial direction antenna array can detect the axial slits more effectively than the circumferential slits. These studies confirmed that the antenna array was feasible to use the linearly polarized TE_{11} mode microwave for pipe crack detection.

Data Availability

The labelled data sets used to support the findings of this study are available from the corresponding author upon request.

Conflicts of Interest

The authors declare no conflicts of interest or personal relationships that could have appeared to influence the work reported in this paper.

Acknowledgments

This work was supported by the National Natural Science Foundation of China (Grant number 62175223), and the Basic Public Welfare Research Program of Zhejiang Province (Grant number LGF19F010003).

References

[1] N. Tsopelas and N. J. Siakavellas, "Eddy current thermography in circular aluminium plates for the experimental verification of an electromagnetic–thermal method for NDT," *Nondestructive Testing and Evaluation*, vol. 25, no. 4, pp. 317–332, 2010.

[2] G. Chen, T. Katagiri, H. Song, N. Yusa, and H. Hashizume, "Detection of cracks with arbitrary orientations in a metal pipe using linearly-polarized circular TE_{11} mode microwaves," *Nondestructive Testing and Evaluation*, vol. 107, article 102125, 2019.

[3] K. Karhunen, A. Seppänen, and J. P. Kaipio, "Adaptive meshing approach to identification of cracks with electrical impedance tomography," *Inverse Problems and Imaging*, vol. 8, no. 1, pp. 127–148, 2014.

[4] T. T. Zhang, Y. F. Tan, X. D. Zhang, and J. H. Zhao, "A novel hybrid technique for leak detection and location in straight pipelines," *Journal of Loss Prevention in the Process Industries*, vol. 35, pp. 157–168, 2015.

[5] W. Peng and F. Adachi, "Capacity of distributed antenna network by using single-carrier frequency domain adaptive antenna array," *Wireless Communications and Mobile Computing*, vol. 14, no. 13, p. 1251, 2012.

[6] M. Doaei and S. M. Tavallali, "Intelligent screening of electrofusion-polyethylene joints based on a thermal NDT method," *Infrared Physics & Technology*, vol. 90, pp. 1–7, 2018.

[7] T. Uchimoto, T. Takagi, T. Ichihara, and G. Dobmann, "Evaluation of fatigue cracks by an angle beam EMAT-ET dual probe," *Nondestructive Testing and Evaluation*, vol. 72, pp. 10–16, 2015.

[8] R. E. Jones, F. Simonetti, M. J. S. Lowe, and I. P. Bradley, "Use of microwaves for the detection of water as a cause of corrosion under insulation," *Journal of Nondestructive Evaluation*, vol. 31, no. 1, pp. 65–76, 2012.

[9] S. F. Gong, X. Xu, and M. Karlsson, "Broadside-coupled microstrip lines as low loss metamaterial for microwave circuit design," *Wireless Communications and Mobile Computing*, vol. 2019, Article ID 9249352, 13 pages, 2019.

[10] Y. C. Yu, A. Safari, X. D. Niu, B. Drinkwater, and K. V. Horoshenkov, "Acoustic and ultrasonic techniques for defect detection and condition monitoring in water and sewerage pipes: a review," *Applied Acoustics*, vol. 183, article 108282, 2021.

[11] K. Imano and M. Kondou, "Detecting pipe wall reduction using air-coupled MHz range ultrasonic wave," *IECE Electronics Express*, vol. 6, no. 10, pp. 613–617, 2009.

[12] X. B. Hong, Y. Liu, X. H. Lin, Z. Luo, and Z. He, "Nonlinear ultrasonic detection method for delamination damage of lined anti-corrosion pipes using PZT transducers," *Applied Sciences*, vol. 8, no. 11, article 2240, 2018.

[13] M. H. Siqueira, C. E. Gatts, R. R. da Silva, and J. M. A. Rebello, "The use of ultrasonic guided waves and wavelets analysis in pipe inspection," *Ultrasonics*, vol. 41, no. 10, pp. 785–797, 2004.

[14] D. Kalhor, S. Ebrahimi, R. B. Tokime et al., "Cavity detection in steel-pipe culverts using infrared thermography," *Applied Sciences*, vol. 11, no. 9, p. 4051, 2021.

[15] N. Pan, S. Jiang, Y. Du, and Z. Hu, "Infrared thermal imaging for intelligent leakage detection in underground integrated pipe corridors," *Journal of Testing and Evaluation*, vol. 48, no. 6, pp. 4503–4515, 2020.

[16] K. Imano and M. Kondou, "Possibilities of nondestructive evaluation of a pipe using air-coupled ultrasonic wave in the MHz range," *IECE Electronics Express*, vol. 5, no. 17, pp. 668–671, 2008.

[17] W. Gao, D. Zhang, and E. Zhang, "Defect detection in the dead zone of magnetostrictive sensor for pipe monitoring," *IEEE Sensors Journal*, vol. 21, no. 3, pp. 3420–3428, 2021.

[18] S.-J. Xie, Z.-R. Duan, J. Li, Z. Tong, M. Tian, and Z. Chen, "A novel magnetic force transmission eddy current array probe and its application for nondestructive testing of defects in pipeline structures," *Sensors and Actuators A: Physical*, vol. 309, article 112030, 2020.

[19] S. Majidnia, J. Rudlin, and R. Nilavalan, "Investigations on a pulsed eddy current system for flaw detection using an encircling coil on a steel pipe," *Insight*, vol. 56, no. 10, pp. 560–565, 2014.

[20] S. M. Mohammadi, L. K. S. Daldorff, J. E. S. Bergman et al., "Orbital angular momentum in radio—a system study," *IEEE Transaction on Antennas and Propagation*, vol. 58, no. 2, pp. 565–572, 2010.

[21] D. D. Liu, L. Q. Gui, K. Chen et al., "Theoretical analysis and comparison of OAM waves generated by three kinds of antenna array," *Digital Communications and Networks*, vol. 7, no. 1, pp. 16–28, 2021.

[22] S. J. Orfanidis, "Electromagnetic wave and antennas," 2004, http://www.ece.rutgers.edu/~orfanidi/ewa.

[23] J. Parker, C. W. P. Eterson, Y. Yifat et al., "Optical matter machines: angular momentum conversion by collective modes in optically bound nanoparticle arrays," *Optica*, vol. 7, no. 10, pp. 1341–1348, 2020.

[24] W. J. Byun, Y. S. Lee, B. S. Kim, K. S. Kim, M. S. Kang, and Y. H. Cho, "Simple generation of orbital angular momentum modes with azimuthally deformed Cassegrain subreflector," *Electronics Letters*, vol. 51, no. 19, pp. 1480–1482, 2015.

[25] K. Sasaki, T. Katagiri, N. Yusa, and H. Hashizume, "Demonstration of the applicability of nondestructive microwave testing to the long-range inspection of inner-surface cracks in tubes," *Materials Transactions*, vol. 58, no. 4, pp. 692–696, 2017.